small methods
www.small-methods.com

ICP–MS Assisted EDX Tomography: A Robust Method for Studying Electrolyte Penetration Phenomena in Gas Diffusion Electrodes Applied to CO_2 Electrolysis

Alain Rieder, Julia Lorenzetti, Iván Zelocualtecatl Montiel, Abhijit Dutta, Anna Iarchuk, Marta Mirolo, Jakub Drnec, Francesca Lorenzutti, Sophia Haussener, Noémi Kovács, Soma Vesztergom, and Peter Broekmann**

Abstract: A carbon paper-based gas diffusion electrode (GDE) is used with a bismuth(III) subcarbonate active catalyst phase for the electrochemical reduction of CO_2 in a gas/electrolyte flow-by configuration electrolyser at high current density. It is demonstrated that in this configuration, the gas and catholyte phases recombine to form K_2CO_3/$KHCO_3$ precipitates to an extent that after electrolyses, vast amount of K^+ ions is found by EDX mapping in the entire GDE structure. The fact that the entirety of the GDE gets wetted during electrolysis should, however, not be interpreted as a sign of flooding of the catalyst layer, since electrolyte perspiring through the GDE can largely be removed with the outflow gas, and the efficiency of electrolysis (toward the selective production of formate) can thus be maintained high for several hours. For a full spatial scale quantitative monitoring of electrolyte penetration into the GDE, (relying on K^+ ions as tracer) the method of inductively coupled plasma–mass spectrometry (ICP–MS) assisted energy dispersive X-ray (EDX) tomography is introduced. This new, cheap and robust tomography of non-uniform aspect ratio has a large planar span that comprises the entire GDE surface area and a submicrometer depth resolution, hence it can provide quantitative information about the amount and distribution of K^+ remnants inside the GDE structure, in three dimensions.

1. Introduction

In order to achieve the ambitious goal of the Paris agreement[1] —namely, to limit the global temperature increase to 1.5 °C above pre-industrial levels— cutting back the emission of greenhouse gases, including carbon dioxide (CO_2), is required. This necessitates the development of sustainable chemical technologies that use electricity from renewable sources to turn CO_2 into value-added products.[2,3] The electrochemical CO_2 reduction reaction (*ec*–CO_2RR) has thus received renewed interest in the past few decades when several new (in particular, metallic) catalysts have been described that can selectively turn CO_2 into some desired products.[4–7] It was found in standard laboratory scale experiments applying classical H-type electrolysis cells, for example, that while on Au, Ag, Zn, Pd, Ga, Ni, and Pt electrode materials carbon monoxide (CO) is the preferred product, on some other metals such as Pb, Hg, In, Sn, Cd, or Tl, *ec*–CO_2RR tends to selectively yield formate ($HCOO^-$).[8,9] For the production of more exotic products (e.g., methane, C_2 hydrocarbons or alcohols), Cu is the most ideal platform.[10]

Although experiments in an H-type cell are considered important in the early stage of electrocatalysis research —and these experiments have indeed often led to the discovery of promising new catalyst materials—[11,12] it is to be emphasised that even the most successful H-type cell

A. Rieder, J. Lorenzetti, I. Zelocualtecatl Montiel, A. Dutta, A. Iarchuk, S. Vesztergom, P. Broekmann
Department of Chemistry, Biochemistry and Pharmaceutical Sciences
NCCR Catalysis, University of Bern
Freiestrasse 3, Bern 3012, Switzerland
E-mail: vesztergom@chem.elte.hu; peter.broekmann@unibe.ch

The ORCID identification number(s) for the author(s) of this article can be found under https://doi.org/10.1002/smtd.202400200

DOI: 10.1002/smtd.202400200

M. Mirolo, J. Drnec
ID31 beamline, Experimental Division
European Synchrotron Radiation Facility (ESRF)
Grenoble France

F. Lorenzutti, S. Haussener
Laboratory of Renewable Energy Science and Engineering
NCCR Catalysis, Swiss Federal Institute of Technology in Lausanne (EPFL)
Station 9, Lausanne 1015, Switzerland

N. Kovács, S. Vesztergom
MTA–ELTE Momentum Interfacial Electrochemistry Research Group
Eötvös Loránd University
Pázmány Péter sétány 1/A, Budapest 1117, Hungary

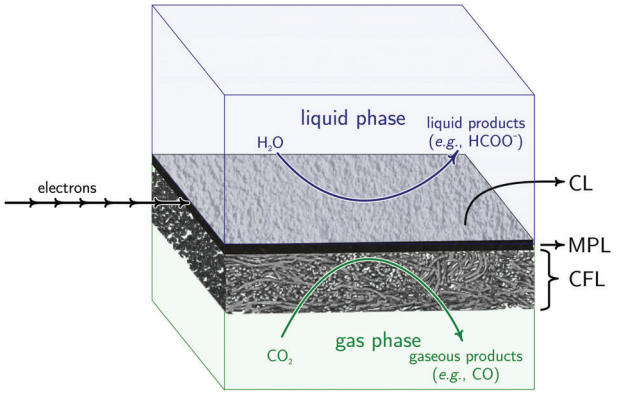

Figure 1. Scheme of a gas diffusion electrode operated as a cathode for *ec*–CO_2RR.

experiments have little if anything to tell about the scale-up prospects of the *ec*–CO_2RR process. This is due to the low solubility of molecular form CO_2 in aqueous environments that easily turns *ec*–CO_2RR transport limited, so that current densities achievable in classical H-type cells often fall short, by several orders of magnitude, the requirements of industry ($\gtrsim 1$~A~cm^{-2}).

For the alleviation of transport limitations, the application of gas diffusion electrodes (GDEs, **Figure 1**) seems to provide a promising solution.[13,14] The core of the GDE is the gas diffusion layer (GDL) that is itself a bi-layer structure formed by a microporous layer (MPL) and a carbon fibrous layer (CFL). The GDL is turned into an actual GDE when a catalyst layer (CL) is applied, for example by spray coating, on top of the MPL. The role of the thin MPL is thus to support the CL, and provide access to the catalyst material for both electrons (the GDL as a whole is thus often made of conductive carbon) and CO_2 molecules (the latter through the micropores of the MPL). In addition, the pores of the MPL also provide means for the formed reaction products to escape the layer, so that their accumulation and hindrance of the on-going reaction is avoided. That CO_2 can approach the MPL close enough is assured by the loose structure of the underlying CFL.

For *ec*–CO_2RR to proceed at high reaction rates, the abundance of all three reactants is to be assured: that is, CO_2 molecules (supplied mostly by the gas phase), H_2O molecules (supplied mostly by the liquid phase) and electrons (supplied by the solid phase) must all be present where the reaction takes place.[15] The function of a well-operating GDE is thus to create three-phase (gas | solid | liquid) boundaries at locations where the catalyst material is present at high concentrations.[16]

In an ideal case, the products of *ec*–CO_2RR should be transported as fast as possible away from the reaction scene. For example, when the product of *ec*–CO_2RR is CO,

$$CO_2 + H_2O + 2e^- \rightarrow CO + 2OH^- \quad (1)$$

CO (a barely soluble gaseous compound) is taken up by the gas phase. If, on the other hand, *ec*–CO_2RR is directed toward the production of formate,

$$CO_2 + H_2O + 2e^- \rightarrow HCOO^- + OH^- \quad (2)$$

$HCOO^-$ ions would remain in the liquid phase.

In order to assure a fast transport of products away from the reaction scene, and also to replenish near-electrode reactant concentrations as quickly as possible, flow conditions (convection) are often applied in practical electrolysers, both in the gas and in the liquid phase.

In an electrolyser,[17–19] the liquid phase of the GDE cathode is interfaced to a membrane (usually an anion exchange membrane, AEM) and through it, to an anode compartment. We note here that in cases where the reduction of CO_2 is not expected to yield any liquid products, the liquid phase can be omitted and the membrane may directly be placed over the catalyst layer. In these so-called zero-gap cathode configurations[20] the amount of water necessary for *ec*–CO_2RR to proceed comes from the anode side of the electrolyser through the wetted membrane.

Practically regardless to whether a CO_2 reducing GDE is operated in a zero-gap or in a fluidic (Figure 1) configuration, ensuring proper electrolyte (water) management of the GDE is paramount in order to uphold stable operation during long-time electrolyses. From this point of view, the over-hydration (or in short, the flooding) of GDEs poses the biggest threat toward system durability.[16,18–38] While the presence of some amount of water in the CL of GDEs is in fact required for *ec*–CO_2RR to proceed, see Equations (1) and (2), over-hydration occurs if excess water floods the entire CL, displacing the afore-mentioned gas | solid | liquid three-phase boundary[15] to deeper parts of the MPL or to the CFL, where no catalyst is present.

During constant current electrolysis, the water blockage of CO_2 reduction sites will result in the onset of parasitic hydrogen evolution reaction (HER):

$$2H_2O + 2e^- \rightarrow H_2 + 2OH^- \quad (3)$$

The cell will fail to reduce CO_2 —the Faradaic efficiency (*FE*) of *ec*–CO_2RR products will immediately drop down— and the cell voltage will increase to anomalously high values. If flooding occurs during constant voltage electrolyses, usually the current drops down to small values, in parallel with the decrease of the *FE* of *ec*–CO_2RR products.

The flooding of gas diffusion electrodes can be caused by a variety of effects (pressure imbalances, gas or liquid flow irregularities) that can however be avoided by a careful optimization of process parameters (flow rates etc.)[18] and by taking precautions that, at least at the start of the electrolysis, the prepared GDEs have a hydrophobic character.[16,18–32]

There is one effect, however, which is hard to avoid, and which will almost definitely cause some electrolyte penetration into the GDE structure: this is the formation of bicarbonate or carbonate precipitates,[23] due to a reaction of CO_2 with the catholyte (usually KOH or some other alkaline compound):

$$KOH + CO_2 \rightarrow KHCO_3 \quad (4)$$

or

$$2KOH + CO_2 \rightarrow K_2CO_3 + H_2O \quad (5)$$

The above reactions can essentially occur at any liquid | gas phase boundary inside the GDE. If K_2CO_3/$KHCO_3$ salts are

formed at concentrations exceeding their solubilities, they are going to precipitate inside the porous structure, and possibly also on top of the applied GDEs. This will eventually start a vicious circle, as due to the formation of precipitates, the original hydrophobicity of the electrode will be gradually decreased, which will result in a further penetration of electrolyte into the GDE, allowing the formation of more precipitates until —probably after not very long operation times— the entire GDE will become wetted to some extent.

At this point it is important, however, to distinguish between the wetting of the GDE (penetration of electrolyte into the GDL structure) and the flooding (overhydration) of the catalyst layer. While several authors interpret electrolyte penetration as a synonym of flooding,[16,18–28] it was pointed out recently that even GDEs that are wetted to an extent that the electrolyte already breaks through them[28–32] can remain fully functional for *ec*–CO_2RR, so that their catalyst layer should hardly be considered "flooded" in the classical sense. In fact, electrolyte droplets in the output gas flow of well operating electrolysers can often be detected — this effect is referred to as seepage,[28] weeping,[31] or (as we will call it) perspiration.[30]

That perspiration should not be interpreted as a sign of flooding in Ag catalyst-based CO producing zero-gap *ec*–CO_2RR reactors, but on the contrary, it is an indication of stable operation of the reactor, was pointed out by some of our recent works[33–37] and is also supported by the work of other researchers.[28–32] In these works it is disputed that electrolyte penetration into the GDE should necessarily be considered as an advent of flooding and of performance break-down, and that it was either necessary or very effective to build several lines of defence —the first being that we assure the non-wettability of the CL—[25] against it. In turn, we argued that such penetration (especially due to the hydrophobicity decreasing effects of precipitate formations) could never be fully avoided, and it was more important to maintain effective exit routes inside the GDE structure, through which the penetrated electrolyte could percolate through, leaving the CL still active and mostly unflooded.[35–37]

In this present work we demonstrate the validity of the above statement for fluidic (as opposed to zero-gap) electrolysers that we use for formate production with an in situ formed Bi(III) subcarbonate active catalyst phase. We show that also in this fluidic cell, the electrolyte penetrates (within relatively short time) the GDE. As, however, the penetrated electrolyte can leave the cathode in the form of aerosol with the gas out-flow, it does not flood the CL — enabling a long-time operation of the electrolyser.

To monitor the amount of catholyte that perspired through the GDE, we apply a liquid trap on the gas out-flow, and demonstrate that during operation of the cell, the K^+ concentration in the trap steadily rises, while the *FE* of formate (that was initially higher than 95%) does not drop below approx. 90%.

In order to gain an insight to the spatial distribution of electrolyte penetration into the GDE structure, we apply different tomographic methods. By considering the local K^+ concentration as a tracer of electrolyte penetration, we demonstrate that synchrotron-based X-ray diffraction computer tomography (XRD–CT, a method that has recently gained popularity in advanced operando electrolysis studies)[38,39] can provide important indications on electrolyte penetration. Information yielded by XRD–CT remains, however, localized in the sense that it corresponds to a small area of the GDE plane. Furthermore, the vertical resolution of K^+ distribution profiles, determined by XRD–CT, will also be limited by measurement time.

To overcome the above limitations, a novel method, inductively coupled plasma mass spectrometry (ICP–MS) assisted energy dispersive X-ray (EDX) tomography was developed. ICP–MS assisted EDX tomography is of non-uniform aspect ratio and it can thus map the penetration of electrolyte over the entire GDE structure with improved depth resolution. Aspiring that it will find further application in the research of various kinds of GDE-based electrolyser systems, the aim of this paper is to give a detailed description of ICP–MS assisted EDX tomography in the form of a case study where we apply the method for the post-electrolysis investigation of formate-producing GDEs bearing a Bi(III) subcarbonate catalyst phase, operated at high current density in a gas/electrolyte flow-by configuration.

2. The Studied System

A sketch of the studied electrolyser (see the Experimental Section for detailed description), with focus on the GDE and its fitting to the current collector (cathode) plate, is shown in **Figure 2** (see Figure S1, Supporting Information for an animated assembly view). In this vertical flow-by configuration, the anolyte and catholyte (1∼moldm^{-3} KOH solutions) both flow upward, driven by a pump, so that no pressure difference is exerted on the anion exchange membrane. To the back-side of the cathode GDE, humidified CO_2 gas is fed in the opposite (downward) direction. The gas outflow is equipped with a water containing trap for the monitoring of K^+ that perspires through the GDE and leaves the electrolyser with the out-flow CO_2 stream.

The applied catalyst was prepared by the dynamic hydrogen bubble templated (DHBT)[40] deposition of a metallic bismuth foam. This foam was crushed and suspended in isopropanol by sonication, then dried and annealed in air to form a Bi_2O_3 catalyst precursor. The precursor was subsequently turned into an isopropanol-based, Nafion containing ink that was spray coated on a commercial Freudenberg H23C8 GDL (see the Experimental Section, as well Section S2, Supporting Information for details).

As shown by the first column of **Figure 3**, the above preparation procedure resulted in a GDE bearing a yellowish Bi_2O_3 catalyst precursor layer, in the microstructure of which dendrites of the oxide could clearly be observed by scanning electron microscopy (SEM). Sessile water drop measurements indicate that the as-prepared catalyst layer is hydrophobic, and both XRD and Raman spectroscopic investigation confirm that the precursor CL contains Bi exclusively in the Bi_2O_3 phase.

Focused ion beam–scanning electron microscopy (FIB–SEM) nanotomography reconstruction (see Figure S3, Supporting Information) shows that the Bi_2O_3 precursor CL has a thickness of about 7 µm, an average particle size of (177±5) nm, a roughness factor of 42.4±0.3 and a solid volume fraction of 0.22±0.01. The material was found to be mostly connected (99.55%±0.02% of the CL is in contact) and anisotropic in the through-plane dimension, with a maximum solid chord length of 2 µm in the through-plane and 3 µm in the in-plane direction.

As indicated by previous studies,[41] when brought into contact with CO_2 gas and alkaline electrolytes, the Bi_2O_3 precursor turns into the $(BiO)_2CO_3$ active catalyst phase, even if no

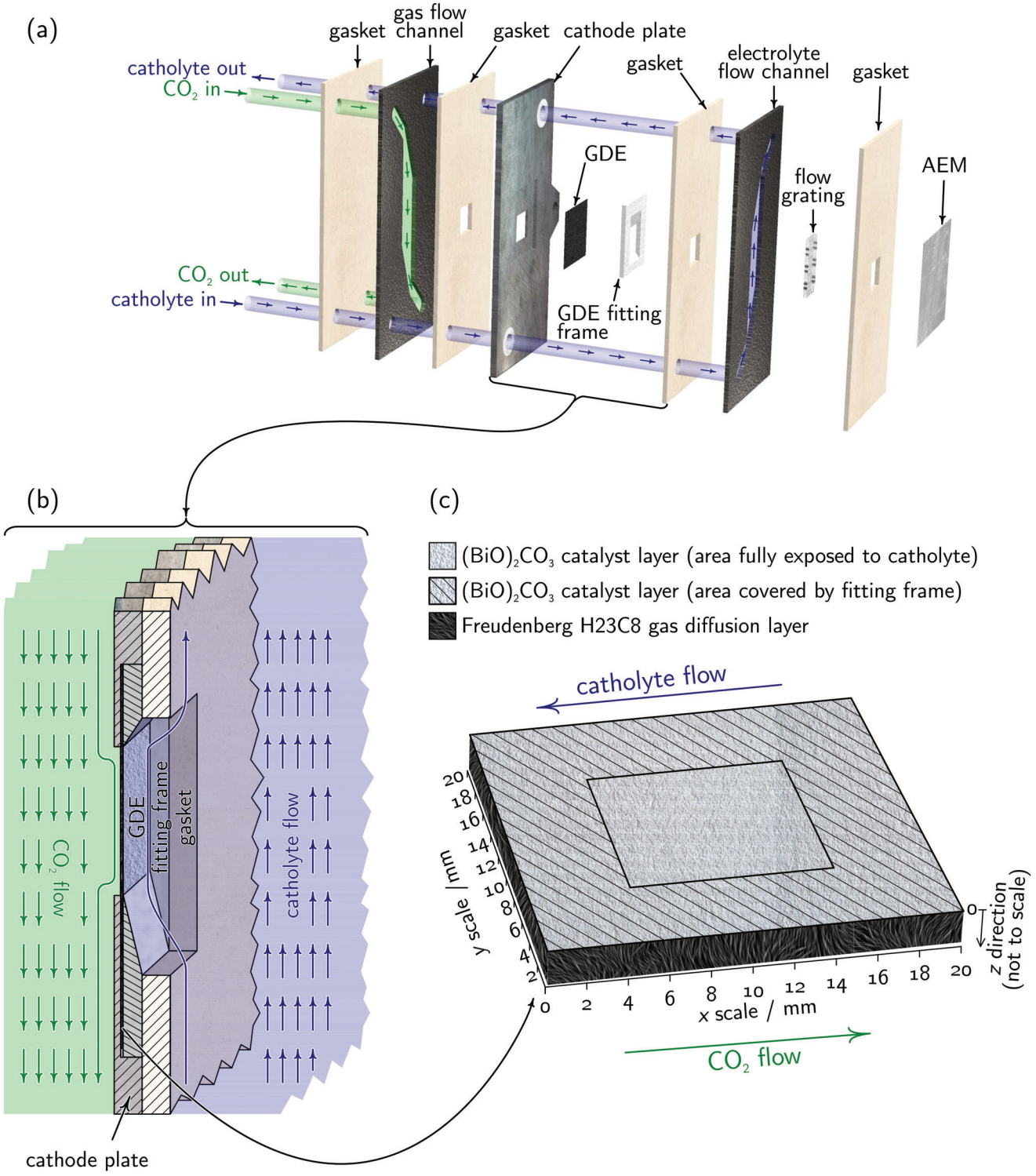

Figure 2. The system under study. The cathode compartment of the electrolyser is shown in (a); the anode compartment, containing a Pt foil anode, is of symmetrical structure. The fitting of the GDE into the current collector (cathode) plate by means of a PTFE fitting frame and a gasket is shown in (b). The GDE, placed in a system of Cartesian coordinates used henceforth, is shown in (c). The dashed area over the GDE surface is covered by the fitting frame, and is not in (direct) contact with the catholyte.

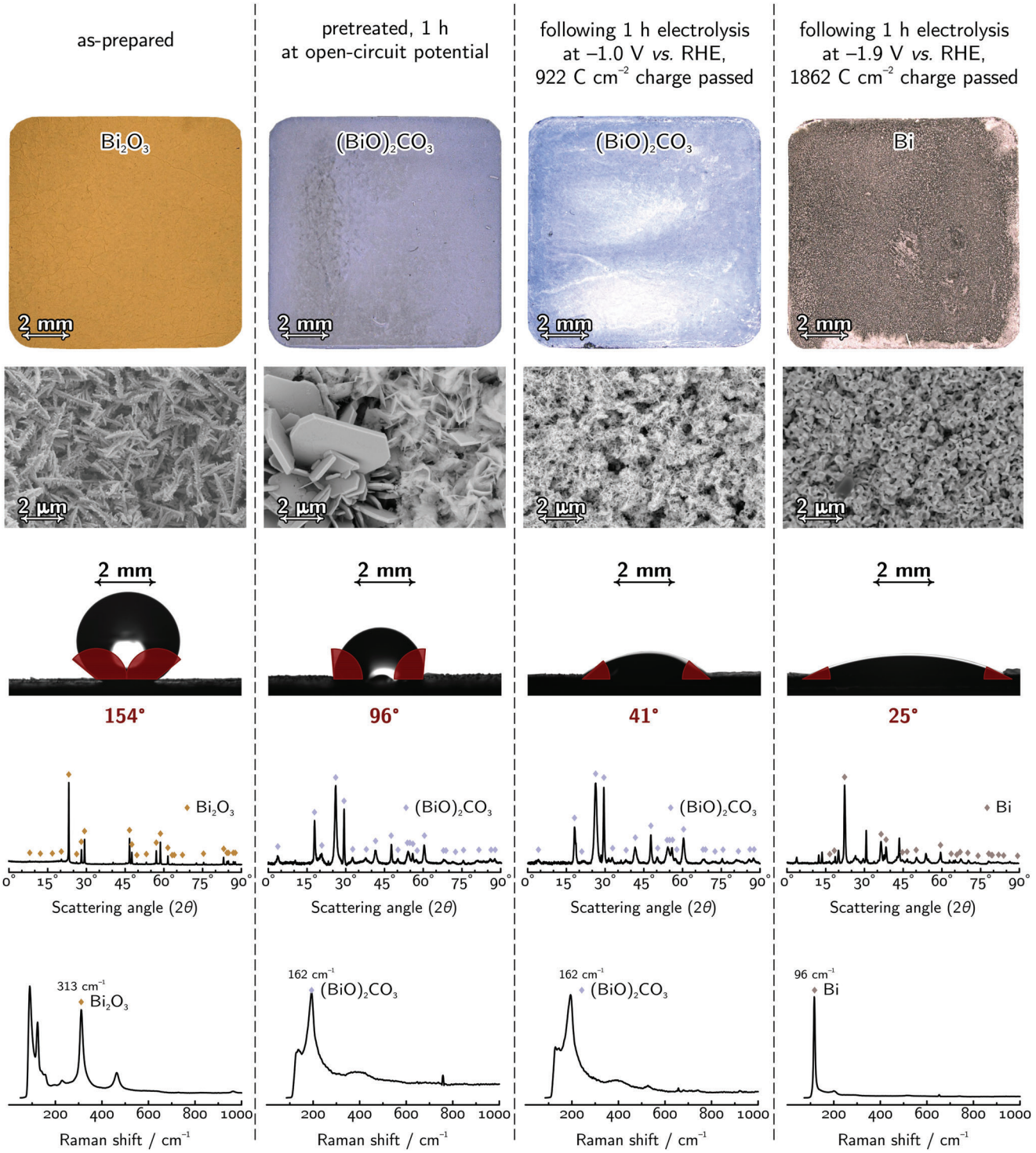

Figure 3. Physical and chemical characterization of the GDE at its different life stages. Photographs (top row), scanning electron micrographs (second row) and sessile water drop measurements (third row) on as-prepared GDEs, as well as on GDEs that underwent pre-treatment (to turn the bismuth(III) oxide to the bismuth(III) subcarbonate phase) or electrolyses at given potentials. X-ray diffractograms (fourth row) and Raman spectra (bottom row) of the catalyst layers clearly indicate that while electrolysis under mild conditions (e.g., at –1.0 V vs. RHE) leaves the subcarbonate phase intact, harsh cathodic conditions (e.g., polarization to –1.9 V vs. RHE) reduce the catalyst to metallic Bi; this reduction is concomitant with the loss of formate selectivity, see Figure S4 (Supporting Information). Colored diamond symbols mark the peaks of the most abundant phase in the X-ray diffractograms and Raman spectra.

negative potential is externally applied to the cathode (second column in Figure 3). The $Bi_2O_3 \rightarrow (BiO)_2CO_3$ transition is marked by the appearance of carbonate crystallites in the SEM image of the catalyst layer that, as indicated by contact angle measurements, still retains its hydrophobicity. Both XRD and Raman spectroscopy confirm that following the 1 hour pretreatment $(BiO)_2CO_3$ is the prevailing phase of the CL.

The composition of the CL remains essentially unchanged if electrolyses not venturing to extremely cathodic potentials are carried out at the GDE. As shown by the third column of Figure 3 following 1 h electrolysis at a mild reducing potential of –1.0 V versus RHE, during which a charge of 922 C cm^{-2} passes through the GDE at a relatively stable current density of about $-256\sim mA\sim cm^{-2}$ (normalised to the 1 cm^2 fully exposed area of the GDE), the hydrophobicity of the CL is decreased. Post-electrolysis X-ray diffractometry and Raman spectroscopy reveals, however, that the phase composition of the $(BiO)_2CO_3$ CL essentially remained intact under these mild operating conditions.

If on the other hand the electrolysing potential is increased to –1.9 V versus RHE, resulting in the passage of 1862 C cm^{-2} at a current density of about $-520\sim mA\sim cm^{-2}$, the hydrophobicity of the CL is lost (fourth column of Figure 3), and both XRD and Raman spectroscopy show that the CL is fully reduced to metallic Bi. At this stage the catalyst already loses its selectivity toward formate production, and the majority of the applied current is misspent for the electrolysis of water (a potential-dependent Faradaic efficiency study is shown in Figure S4, Supporting Information).

As a consequence of the above-described screening experiments, during our studies we refrained from exposing the cathode to overly negative potentials, and we applied a 145 mA cm^{-2} constant current density (normalized to the 1 cm^2 fully exposed area of the GDE) during all subsequent electrolysis experiments. Prior to the electrolyses, the CO_2 and electrolyte flows were turned on for a duration of 1 h, without the application of current, in order to make sure that the $(BiO)_2CO_3$ active catalyst phase is formed, and all electrolysis experiments are started from the same initial state. All the conducted galvanostatic electrolyses took place in a $1\sim moldm^{-3}$ KOH catholyte since, as shown in Figure S5 (Supporting Information), increasing the catholyte concentration to for example $5\sim moldm^{-3}$ already causes system instabilities in short time due to the massive formation of $K_2CO_3/KHCO_3$ precipitates, even on the fibrous side of the GDE.

As shown in **Figure 4a**, the Faradaic efficiency of $HCOO^-$ production drops only negligibly from an initial value of 95% to about 90% during the approximately 4 h long electrolysis, during which the cathode potential changes only negligibly, from approximately –0.8 to –1.0 V versus RHE (see Figure 4b). As was indicated by potentiostatic screening experiments (see Figure S4, Supporting Information for details), the $(BiO)_2CO_3$ phase is stable at these potentials, and the reduction of the catalyst to metallic Bi can essentially be avoided throughout the entire electrolysis.

As indicated by ICP–MS measurements (see Figure 4c), during the course of electrolysis the catholyte seems first to penetrate and then to saturate the GDE structure. This penetration causes, however, no apparent stability issues, since a big portion of the permeated catholyte leaves the GDE and ends up in the liquid trap equipped to the gas out-flow of the cathode chamber (Figure 4d).

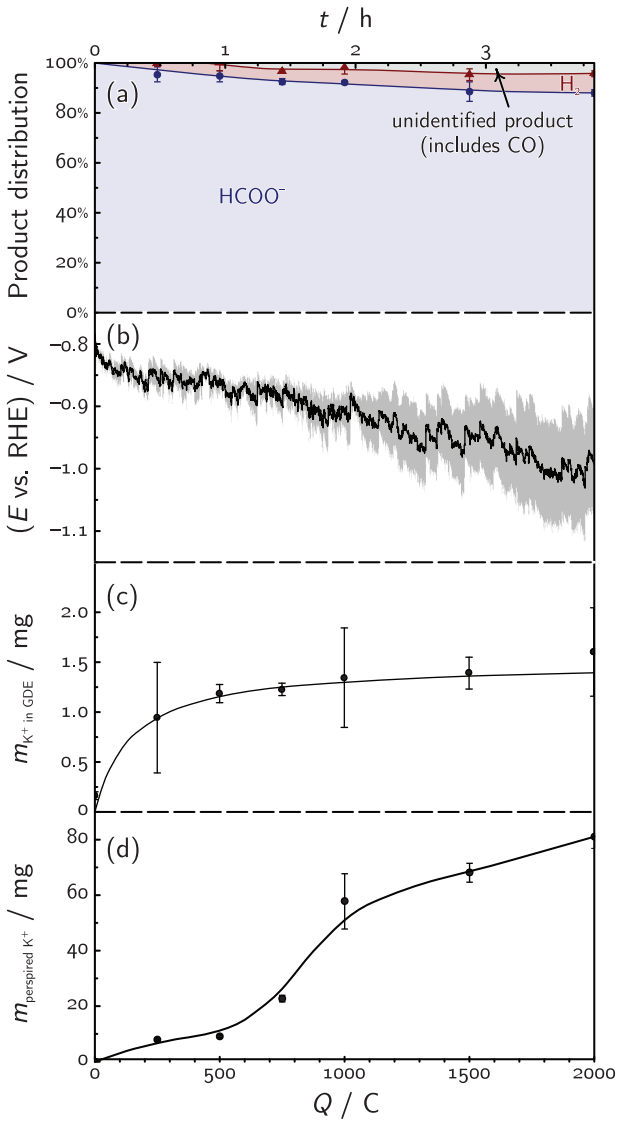

Figure 4. Results of long-term electrolysis on $(BiO)_2CO_3$-covered GDE. Panel (a) shows the product distribution of the electrolysis, panel (b) the recorded potential transient, panel (c) the amount of K^+ accumulated within the GDE structure and panel (d) the cumulative amount of K^+ that perspired through the cell. Data points show the average of three independent measurements, the curves were created by spline interpolation for panels (a), (c) and (d). The curve in panel (b) shows the average of three independent measurement, with the shaded area representing the 95% confidence band.

3. Monitoring Electrolyte Penetration into the GDE by ICP–MS Assisted 2D EDX Mapping

Determining the K^+ content of GDEs at different stages of the electrolysis (this can be done, e.g., by integrating the ICP–MS determined K^+ profiles shown in Figure S7, Supporting Information) can give direct proof of electrolyte penetration into the GDE structure (see the curve of Figure 4c), yet the application

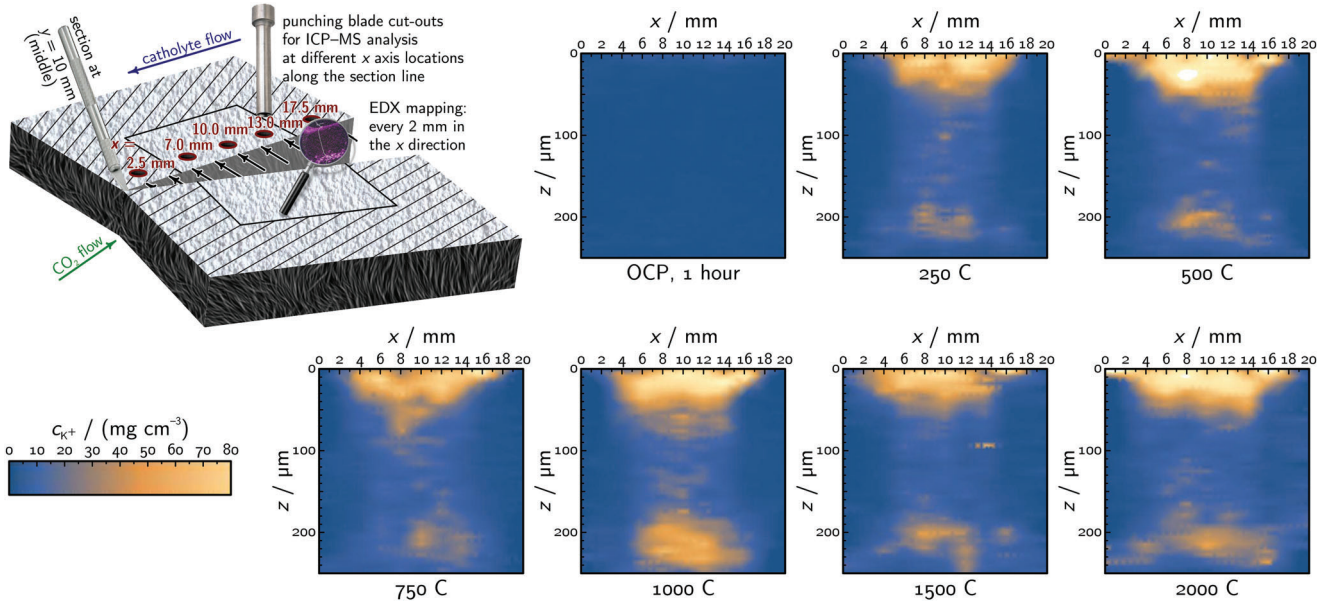

Figure 5. Illustration of the ICP–MS assisted 2D EDX mapping method applied for the monitoring of electrolyte penetration into the GDE structure, and the obtained, quantitatively comparable K^+ densitograms at $y = 1$ cm with the CL located at $z = 0$. See Figure S9 (Supporting Information) for a timeline animation of the evolution of densitograms.

of ICP–MS alone yields no information with regard to the spatial distribution of K^+ salts (that is, the distribution of electrolyte penetration) inside the GDE structure. EDX elemental mapping of GDE cross-sections can deliver such information, especially if, as indicated by the scheme of **Figure 5**, we record elemental maps at given locations along a GDE that was previously cut in the middle by a sharp scalpel. We note here that, contrary to the illustration shown in Figure 5, in order to avoid the smearing of precipitates,[36] this cutting is to be made by applying the scalpel to the CFL side of the GDE.

From elemental maps corresponding to different locations on the x scale (see **Figure 6**), relative K^+ concentration depth (z) profiles can be created in a relatively simple process; that is, i) by summing up pixel values row-by-row; ii) by performing a suitable baseline (background noise) removal on the resulting curve; iii) by determining the location of $z = 0$ using a suitable intensity threshold limit; and iv) by assigning z values to row indices based on the spatial resolution of the original image. The thus obtained depth (z scale) dependent intensity profiles can in a subsequent step be converted to absolute concentration profiles if the surface-normalized absolute K^+ concentrations were known at all x scale locations of EDX profiling.

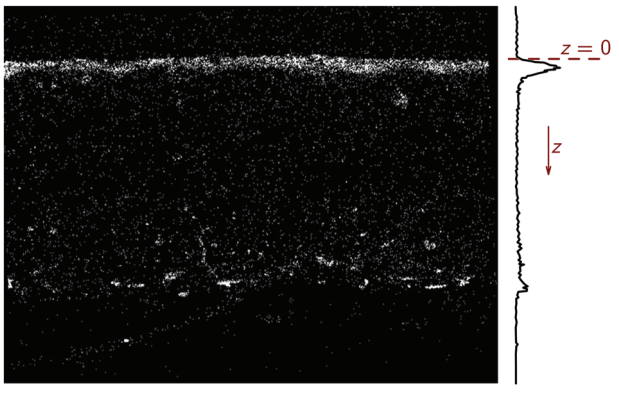

Figure 6. A cross-sectional elemental (K) map of a GDE created by EDX, and a corresponding relative concentration depth profile.

This latter information can be obtained by punching out small segments of the GDE (also shown in Figure 5) and determining their K^+ content by ICP–MS, thus creating by means of interpolation as shown in Figure S7 (Supporting Information), a K^+content (expressed, e.g., in µg cm^{-2}) versus x function that can serve as an integral norm of the EDX-based profiles. The EDX-based (now already absolute) K^+ concentrations can then be plotted as a function of the x and z coordinates, as shown in the density plots of Figure 5. Calculations presented here were carried out by a simple Wolfram Mathematica script, taking ICP–MS measurements and EDX records corresponding to different x scale coordinates as an input. This script is shared using Zenodo[42] in the form of a Mathematica notebook file, but it is also presented and explained in details in the Supporting Information.

The densitograms of Figure 5 (see also Figure S8, Supporting Information for an array of scaled source images) amply demonstrate that the application of current is necessary for electrolyte to penetrate the GDE: following 1 h long operation at open circuit potential (OCP), essentially no K^+ can be detected in the GDE. Following electrolyses at a constant current density of $-145\sim mA\sim cm^{-2}$, the penetration is however obvious, and the amount of detected K^+ grows with the time (charge) of electrolysis. The density plots of Figure 5 further reveal (see Figure S9, Supporting Information for an animated timeline view) that while at earlier stages of the electrolysis the penetration mostly occurs in the direction perpendicular to the GDE surface, at longer electrolysis times also the fitting frame-covered area of

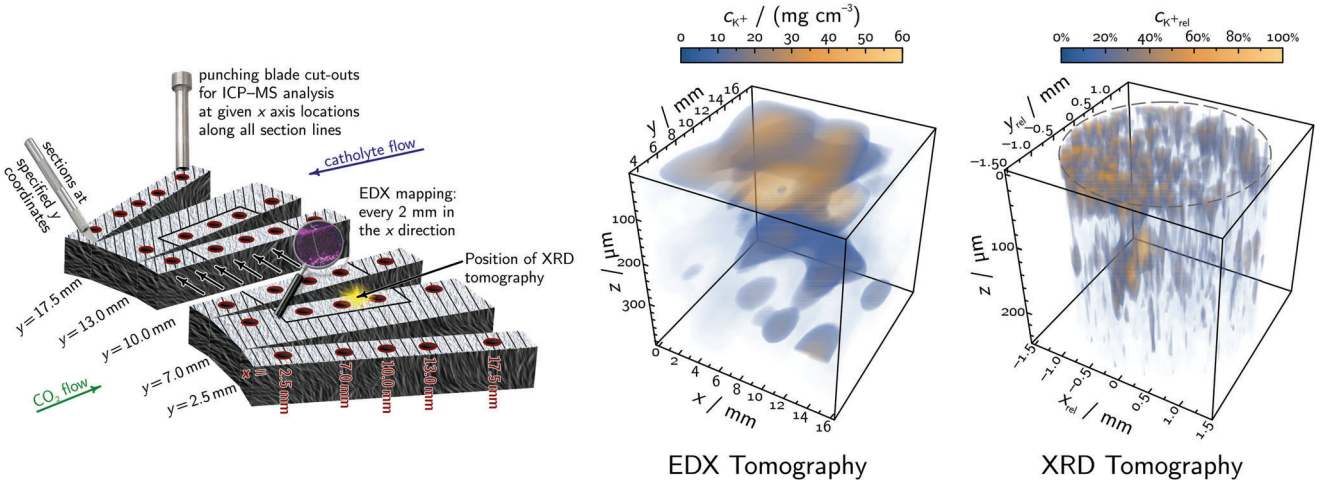

Figure 7. Illustration of the working strategy of the ICP–MS assisted EDX tomography method applied for the monitoring of electrolyte penetration into the GDE structure, and the obtained EDX tomography image. This non-uniform aspect ratio tomogram is compared to an XRD–CT image, taken from one specific spot of the GDE sample, shown in the scheme to the left (note the different scaling of the EDX and XRD tomograms). The studied GDE underwent an electrolysis consuming 750 C of charge before it was cut according to the pattern shown to the left, and made subject to EDX and ICP–MS sampling. See Figure S10 (Supporting Information) for the *x*–*y* dependence of surface area-normalized, ICP–MS-based K^+ concentrations; as well as Figure S11 (Supporting Information) for a rotating (animated) version of the EDX and XRD tomograms.

the GDE gets wetted, resulting in a modest increase of parasitic hydrogen evolution (Figure 4a).

4. Visualizing Electrolyte Penetration in 3D: ICP–MS Assisted EDX Tomography

The bone-shaped catholyte penetration pattern revealed by the 2D densitograms of Figure 5 can also be visualized in three dimensions, if we extend EDX (and ICP–MS) sampling positions, apart from different *x*, also to different *y* scale coordinates as shown by **Figure 7** for a GDE sample that was previously made subject to electrolysis consuming 750 C. The tomogram we obtain by this process is an interpolated form of a pointwise representation of an $\mathbb{R}^3 \to \mathbb{R}$ (that is, $(x, y, z) \to c_{K^+}$) function that can be visualized in the form of a 3D density plot, as shown in Figure 7. We note here that the treatment of individual EDX-based depth profiles, as well as their ICP–MS-based normalization remains essentially the same as presented in the previous section, see the Wolfram Mathematica scripts uploaded to Zenodo[42] and fully documented in the Supporting Information. The only difference is that this time, we use bivariate interpolation in order to determine the *x*–*y* dependence of the ICP–MS-originated surface area normalised concentrations that are used for the integral normalisation of EDX-based intensity profiles (see Figure S10, Supporting Information for details).

Along with the ICP–MS assisted EDX tomography image Figure 7 also presents a synchrotron-based XRD tomogram (see the Experimental Section, as well as Section S8, Supporting Information). Differences of the two methods can readily be seen in this figure. The XRD tomogram has a close-to-unity aspect ratio with fine (about 25 µm, determined by the beam size) resolution in the *x*–*y* plane and a coarser (about 50 µm) *z*-scale resolution. Thus, as depicted also in the sampling scheme of Figure 7, the XRD tomogram corresponds to a relatively small spot of the GDE. In contrast to this, ICP–MS assisted EDX tomography can, depending on the sampling locations, cover a large (in this case 2 cm · 2 cm) span in the *x*–*y* plane, and although this comes at the cost of reduced (2–3 mm) transverse resolution, a fine (about 2 µm) resolution is achieved in the *z* direction.

Due to this far-from-unity aspect ratio, EDX tomography is able to map the penetration of electrolyte into the GDE remarkably well. In Figure 7 it can be seen that it is mostly the upper layer of the GDE (close to the CL) that gets wetted by the electrolyte, although a significant amount of K^+ ions funnels through, and wets also the opposite (CFL) side of the GDE. This "perspiration pathway", as shown by system stability studies (Figure 4) seems essential to uphold the long-time performance of the CO_2-to-formate electrolysis. The apparent bone-shaped penetration pattern, already seen in Figure 5, is probably due to the shading effect of the fitting frame applied to hold the GDE in-place, reducing its active surface area.

With regard to the comparison of EDX and XRD tomographies in Figure 7 we also add that to probe the same volume as ICP–MS assisted EDX tomography, XRD–CT would require unrealistically long, costly synchrotron time: EDX tomography is thus a considerably cheaper method. Nevertheless, XRD–CT still has the considerable advantage that it can be used for the *operando* investigation of heterogeneities in flooding dynamics.[38] ICP–MS assisted EDX tomography obviously lacks this feature, and its application also requires skill both in segmenting the GDE for EDX mapping and in collecting the punching blade cut-outs for ICP–MS measurements.

5. Conclusion

In order to up-scale the performance of *ec*–CO_2RR —the goal is to achieve stable operation at current densities close to the range of 1 A cm^{-2}— the application of GDEs is a straightforward approach. Most GDE-based electrolysers are, however, prone to serious stability issues and most researchers of the field agree[16,18–38]

that these are mostly related to the flooding of the catalyst layer, during operation, by the employed catholyte. If the catalyst particles are flooded by water, they cannot any more be reached by the reactant CO_2 and this does not only hinder the efficiency of the *ec*–CO_2RR process, but also enables unwanted parasitic reactions (mostly, hydrogen evolution).

While consensus seems to exist amongst researchers that flooding (overhydration of the catalyst layer) should necessarily cause a performance breakdown, and efforts should thus be made to avoid this effect, the exact meaning of the term flooding is often not exactly clarified in literature. The penetration of liquid catholyte into the GDE structure is traditionally interpreted as a synonym of flooding, and electrolyte penetration as a whole is thus considered a threat toward electrolyser stability by various researchers. Nonetheless, some published works also hint to that the penetration of electrolyte into the GDE structure should not necessarily be interpreted as flooding, and that some electrolysers can remain fully functional for *ec*–CO_2RR even with GDEs wetted to a great extent.[28–37] We believe that the explanation of this paradox lies in that in certain GDE structures electrolyte can not only enter (so that its accumulation should necessarily lead to the flooding of the CL), but it can also leave, in the form of aerosol droplets, with the outward gas stream. This requires that the electrolyte perspires through the GDE — an effect that we have already indicated in previous works on so-called zero-gap electrolyser designs.[33–37]

In this present paper we studied electrolyte penetration effects into GDEs that were, as opposed to the previously used zero-gap configuration, applied in a vertically placed gas/electrolyte flow-by mode for electrochemical CO_2-to-formate reduction on an in situ formed bismuth(III) subcarbonate active catalyst phase. In this configuration the gas and catholyte phases recombine to form K_2CO_3/$KHCO_3$ precipitates and thus a significant amount of K^+ ions can be detected throughout the entire GDE structure.

By interpreting the emergence of K^+ ions as a tracer of electrolyte penetration we presented a new method of investigating the electrolyte management of CO_2 reducing GDEs operated with an alkaline catholyte phase. Based on the collection of cross-sectional EDX maps, the quantification of these using concentration determination by ICP–MS, and a subsequent visualization of the concentration profiles in multiple spatial dimensions we created a special form of tomography that can find useful application in electrocatalysis research. The new method of ICP–MS assisted EDX tomography was presented in the paper in details. In the hope that other researchers will find it useful, we also published Wolfram Mathematica scripts along with this paper[42] to assist in creating tomography images from sets of ICP–MS and EDX measurements. The commented code is also presented and explained in the Supporting Information.

6. Experimental Section

GDE Preparation: GDEs were fabricated in a three-step process, as shown in Figure S2 (Supporting Information). First, a dendritic Bi foam was prepared by using the DHBT electrodeposition method.[40] The electrodeposition took place in a 100 cm^3 bath that contained ammonium bismuth citrate (Sigma–Aldrich, purity ⩾99.5%) in 20 ~mmoldm^{-3} and sulphuric acid (diluted from 96% H_2SO_4, ACS grade, Sigma–Aldrich) in 1.5 ~moldm^{-3} concentration. A Cu foil cathode substrate with 1 cm^2 geometric area and an 5 cm · 2 cm Pt foil anode were used for the galvanostatic deposition of the Bi foam, which took 60 s at a current density of 3 A cm^{-2}. The prepared Bi foam was then washed with high-purity MilliQ water (specific resistance of 18.2 MΩ cm, total organic carbon content below 5 ppb, Millipore). As shown in Figure S2 (Supporting Information), the foam was characterised by a macroporous structure with dendritic (microporous) walls.

In the second step, the cleaned copper-supported Bi foam was transferred into a vial containing 3 cm^3 isopropanol (BASF SE, assay ⩾99.0%) to detach the porous material from the Cu foil by ultrasonication. The resulting Bi suspension was dried using an oil bath at 100 °C for 20 min, as a result of which, a metallic Bi powder was obtained. This solid was placed in a tube furnace (Nabertherm, Germany) and oxidized to yellow Bi_2O_3 by exposure to air at 350 °C for 8 h, as shown in Figure S2 (Supporting Information).

As a last step, 95 mg of the Bi_2O_3 powder was suspended in a mixture of 19.89 cm^3 isopropanol and 0.11 cm^3 Nafion 117 perfluorinated resin solution ($w_{Nafion} = 5\%$ and $15\% \leq w_{H_2O} \leq 20\%$ in a mixture of lower aliphatic alcohols, Sigma–Aldrich). The thus obtained catalyst ink was sonicated for 25 min at ambient conditions and subsequently spray coated on a commercial GDL (Freudenberg H23C8) with an airbrush pistole (Master Airbrush, G233) propelled by 1 bar nitrogen gas (99.999%, Carbagas, Switzerland). The 20 cm^3 catalyst ink was distributed on a 6.3 cm · 6.3 cm area of the GDL, which resulted in a (nominal) mass loading of 1.25 mg cm^{-2} for Bi. The obtained GDE was cut with a scalpel into segments according the size of the fixation ring of the current collector (2 cm · 2 cm, see Figure 2).

Construction of the Flow Cell Reactor: For electrochemical studies, the GDE was mounted in the cathode current collector of a three-compartment flow cell electrolyser (Electro-Cell, Denmark) the current collector, the fixation ring and the flow fields of which were adjusted according to Figure 2 so that direct contact between the cathode plate and the catholyte was avoided, and system stability was thus increased. The flow channels of the cathode and anode compartments were separated by an anion exchange membrane (Sustainion X37-50 Grade RT membrane). The anolyte and catholyte (both 1~moldm^{-3} KOH, reagent grade, Sigma–Aldrich) were transported through the two flow fields by a peristaltic pump (LabV1, SHE–LabV1–MC4). On the back side of the GDE, humidified CO_2 gas (Carbagas, 99.9999%) was fed with a flow rate of 25 cm^3 min^{-1} through the gas flow channel. The gas flow was precisely controlled with a mass flow controller unit (Vögtlin Instruments GmbH, type GSC–A9SABB2). The gas outflow was equipped with a water containing trap (volume of water: 5 cm^3) for the monitoring of K^+ that perspires through the GDE and leaves the electrolyser with the out-flow CO_2 stream. A Pt foil with a geometric surface area of 1.5 cm^2 was employed as anode of the electrolyser, and a leakless Ag | AgCl | 3~moldm^{-3} KCl reference electrode (eDAQ) could be connected to the catholyte compartment for potential measurements. For comparability, all reported potentials were re-scaled to the RHE scale according to Equation (6):

$$E_{vs.\ \mathrm{RHE}} = E_{vs.\ \mathrm{Ag\ |\ AgCl\ |\ 3\ mol\ dm^{-3}\ KCl}} + 210\ \mathrm{mV} + 59.1\ \mathrm{mV} \cdot p\mathrm{H}. \quad (6)$$

Potentiostatic or galvanostatic control was carried out by an ECi-200 potentiostat (Nordic Electrochemistry, Denmark); all reported potentials were made subject to ohmic drop correction, based on single-frequency impedimetric determination of the high-frequency cell resistance.

Determination of Electrolysis Products: Gaseous reaction products (CO and H_2) were directly analyzed and quantified with online gas chromatography (GC). Volatile products were transported with the constant CO_2 flow to the chromatograph (8610C, SRI Instruments) equipped with a packed Hayesep D and a packed Molesieve 5A column. Ar (99.9999%, Carbagas) was used as carrier gas for the GC analysis. For the quantification of gaseous CO and H_2 electrolysis products, a flame ionization detector coupled to a methaniser and a thermal conductivity detector were applied, respectively. The partial current density j_i corresponding to the formation of a product *i* was determined from Equation (7):

$$I_i = \frac{x_i\, n_i\, \nu\, F}{V_m} \quad (7)$$

and the *FE* of CO or H_2 production was determined as a ratio of the partial currents and the *I* total current of electrolysis:

$$FE_{\text{CO or H}_2} = \frac{I_{\text{CO or H}_2}}{I} \quad (8)$$

where $F = 96485.3$ C mol $^{-1}$ is Faraday's constant, ν is the volumetric gas flow, $V_m = 24.46$ dm^3 mol^{-1} is the molar volume of the gas at ambient conditions, x_i is the mole fraction of component i in the gas flow, and n_i is the number of electrons required by the formation of the product i ($n_{H_2} = n_{CO} = 2$). Aqu eous *ec*–CO_2RR products (the only detectable product in our case was formate) were accumulated in the catholyte (and, due to membrane cross-over, partially in the anolyte) during the electrolysis, and quantified post-electrolysis by an ion chromatograph (Metrohm, 940 Professional IC Vario) equipped with a Metrosep A Supp 7 column. A 3∼mmoldm^{-3} Na_2CO_3 eluent (prepared from anhydrous powder, Sigma–Aldrich) was used combined with a 0.1∼moldm^{-3} H_2SO_4 (prepared from cc. H_2SO_4, BASF SE, Ludwigshafen) suppressor, resulting in a background conductivity of <1.2 µS cm^{-1}. For the calibration of the IC instrument, known standard formate concentration solutions were prepared in the range of 1 to 100 ppm by dilution of a 1000 ppm IC standard solution (Sigma–Aldrich). Prior to IC analysis, the electrolyte samples were diluted (15 to 30-fold) with the eluent, in order to inhibit matrix effects arising from the concentrated KOH electrolyte. The Faradaic efficiency of formate was determined from Equation (9) as

$$FE_{\text{HCOO}^-} = \frac{F\, n_{\text{HCOO}^-} \left(w_{\text{formate in cath}}\, \varrho_{\text{cath}}\, V_{\text{cath}} + w_{\text{formate in an}}\, \varrho_{\text{an}}\, V_{\text{an}}\right)}{Q\, M_{\text{formate}}} \quad (9)$$

where w_{formate}, ϱ and V stand for the weight fraction of formate in, as well as the density and the volume of the catholyte (cath) and the anolyte (an), respectively; Q denotes the total charge of electrolysis, and $M_{\text{formate}} = 45.02$ g mol^{-1} is the molar mass of formate. As both the catholyte and the anolyte are 1∼moldm^{-3} KOH solutions, $\varrho_{\text{cath}} = \varrho_{\text{an}} = 1.05$ g cm^{-3}.

Quantification of Electrolyte Penetration into and Perspiration Through the GDE: For the quantitative determination of the amount of K^+ that perspired through the GDE during an electrolysis experiment, or that remained inside the GDE structure, ICP–MS analysis was applied (NexION 2000 ICP–MS instrument, Perkin Elmer). For this purpose, aliquots from the water trap equipped to the gas outflow of the electrolyser were taken, or GDE segments were cut out and dissolved in concentrated HNO_3 (69.3%, BASF SE, Ludwigshafen).

SEM and EDX Analysis: The SEM and EDX analysis of GDE samples was carried out by using a Zeiss Gemini 450 scanning electron microscope with both InLens secondary electron and back-scattered electron detectors. The EDX cross-section mapping was conducted with an acceleration voltage of 20 kV, a current of 100 pA, and a working distance of 6.8 mm. The position in the cross-section was measured with an internal scale and each elemental mapping was measured with a 200 times magnification.

FIB–SEM Nanotomography: Following sample embedding in epoxy, the material was repeatedly milled with an ion beam and the exposed cross-sections were imaged via SEM. Nanotomography experiments were carried out on a Zeiss NVision 40 CrossBeam instrument (electron beam: Zeiss Gemini, 1–30 kV, 1 nm @ 30 kV, 2.5 nm @ 1 kV; ion-beam: 1–30 kV Ga liquid metal ion source, 4 nm @ 30 kV). The resolution of the tomography was 8 nm and isotropic, and a total volu me of 1464 µm^3 was acquired. Stacks of back-scattered electron images from the tomography experiments were converted into digitalised material through a segmentation process: images were aligned, contrast was balanced, an ideal threshold for segmentation was selected and a 3D morphological opening operation (structuring element $d = 3$ voxels) was performed to smooth the surface of the materials. An aggressive and a conservative threshold were selected as well in order to calculate confidence intervals for the morphological characterization results. The average particle size was calculated by morphological opening with increasingly big spherical structuring elements, until the solid volume fraction was zero, to obtain the opening size distribution as a function of the structuring element diameter. The average diameter of particles was readily extrapolated. The total surface area was obtained via the Matlab function "isosurface", and the roughness factor was calculated by normalizing for the geometrical area. The solid volume fraction was calculated by counting the voxels assigned to Bi_2O_3 and dividing by the total number of voxels in the dataset. The percentage of connected volume was obtained via a watershed algorithm considering 16-connectivity. Chord length distribution was obtained by measuring the length of the chords of the materials, going from one void-solid interface to the next solid-void interface. The operation was repeated along the three Cartesian directions in order to quantify the anisotropy of the material. The segmentation procedure and subsequent morphological analysis were performed in Matlab2017b.[43]

Synchrotron-Based XRD–CT Measurements: Synchrotron-based XRD–CT measurements were performed at the high-energy beamline ID31 of the European Synchrotron Radiation Facility in Grenoble, France. The X-ray beam was monochromatized by a Laue monochromator to an energy of 80 keV and focused to an approximately 6 µm · 20 µm area of the sample. 2D XRD patterns were collected with a Dectris Pilatus 2 M CdTe detector and radially integrated by the pyFAI software.[44] Each slice was reconstructed from 62500 diffraction patterns using a standard back-projection algorithm. Five slices for each sample were spaced by 50 µm to cover the whole volume of the CL.

XRD Characterization of GDEs: To identify different catalyst phases by (lab-based) XRD, an STOE Stadi system equipped with a Cu Kα radiation source ($\lambda = 0.1540$ nm, 40 mA) was used. This system was operated at an acceleration voltage of 40 keV and the resulting X-ray diffractograms were recorded in reflection mode (Bragg–Brentano geometry) in steps of 1° min^{-1} with 2θ values ranging from 0° to 90°. Commercial samples of β-Bi_2O_3 (Sigma–Aldrich, purity ⩾99.8%) and $(BiO)_2CO_3$ (Alfa Aesar, purity ⩾98.5%) were utilized as internal references to assign the diffraction peaks. The measured XRD patterns were analyzed and compared with corresponding data from the International Centre for Diffraction Data powder diffraction files for polycrystalline Bi, Bi_2O_3, and $(BiO)_2CO_3$ (file № 44–1246, 41–1449, and 41–1488).

Raman Characterization of GDEs: Raman spectroscopic analyses (ex situ) were conducted using a LabRAM HR800 confocal microscope (Horiba Jobin Yvon). Spectral data were collected with the Lab Space 3.0 software via the Raman spectrometer coupled with a confocal microscope (Horiba Jobin Yvon). Calibration was carried out using a silicon wafer standard (520.6 cm^{-1}). A large working distance objective lens (50-fold magnification, 8 mm focal length) was applied with a numerical aperture of 0.1 in order to focus a diode-pumped solid-state laser beam (532 nm excitation wavelength, 3 mW power) on the sample and collect the incident and scattered laser light.

Surface Wettability Measurements: The hydrophobicity of the GDE at different stages was analyzed by contact angle measurements. A DSA25 Krüss Advance Drop Shape Analyzer device (Krüss GmbH, Hamburg, Germany) was employed and the measurements were done using freshly prepared GDE and washed electrodes. These specimens were mounted on a mechanical 2D stage, and 5 µℓ Milli-Q water droplets were placed on top of the GDE under ambient conditions with a syringe.

Statistical Analysis: Error bars and confidence bands shown in all Figures correspond to 95% certainty, calculated (unless otherwise noted) by a statistical analysis of the results of at least three independent measurements.

Supporting Information

Supporting Information is available from the Wiley Online Library or from the author.

Acknowledgements

This publication was created as part of NCCR Catalysis (Grant number 180544), a National Centre of Competence in Research funded by the Swiss National Science Foundation. S.V. acknowledged support from the National Research, Development and Innovation Office of Hungary

(NKFIH grant FK135375) and from the Momentum Programme of the Hungarian Academy of Sciences (grant LP2022–18/2022). The authors were indebted to the mechanical workshop, especially to Sandra Hostettler, of the University of Bern for carrying out all necessary modifications to the applied electrolyser cell.

Open access funding provided by Universitat Bern.

Conflict of Interest

The authors declare no conflict of interest.

Data Availability Statement

The data that support the findings of this study are openly available in Zenodo at https://doi.org/10.5281/zenodo.10050308, reference number [42].

Keywords

EDX tomography, electrochemical CO_2 reduction, electrolyte penetration, flooding, gas-fed fluidic electrolyser, perspiration

Received: February 7, 2024
Revised: June 7, 2024
Published online:

[1] United Nations Framework Convention on Climate Change, The Paris agreement, **2015**.
[2] A. I. Osman, M. Hefny, M. I. A. A. Maksoud, A. M. Elgarahy, D. W. Rooney, *Environ. Chem. Lett.* **2020**, *19*, 797.
[3] M. Bui, C. S. Adjiman, A. Bardow, E. J. Anthony, A. Boston, S. Brown, P. S. Fennell, S. Fuss, A. Galindo, L. A. Hackett, J. P. Hallett, H. J. Herzog, G. Jackson, J. Kemper, S. Krevor, G. C. Maitland, M. Matuszewski, I. S. Metcalfe, C. Petit, G. Puxty, J. Reimer, D. M. Reiner, E. S. Rubin, S. A. Scott, N. Shah, B. Smit, J. P. M. Trusler, P. Webley, J. Wilcox, N. MacDowell, *Energy Environ. Sci.* **2018**, *11*, 1062.
[4] M. G. Kibria, J. P. Edwards, C. M. Gabardo, C.-T. Dinh, A. Seifitokaldani, D. Sinton, E. H. Sargent, *Adv. Mater.* **2019**, *31*, 1807166.
[5] K. Wiranarongkorn, K. Eamsiri, Y.-S. Chen, A. Arpornwichanop, *J. CO2 Util.* **2023**, *71*, 102477.
[6] K. C. Poon, W. Y. Wan, H. Su, H. Sato, *RSC Adv.* **2022**, *12*, 22703.
[7] S. Nitopi, E. Bertheussen, S. B. Scott, X. Liu, A. K. Engstfeld, S. Horch, B. Seger, I. E. L. Stephens, K. Chan, C. Hahn, J. K. Nørskov, T. F. Jaramillo, I. Chorkendorff, *Chem. Rev.* **2019**, *119*, 7610.
[8] Y. Hori, H. Wakebe, T. Tsukamoto, O. Koga, *Electrochim. Acta* **1994**, *39*, 1833.
[9] Y. Hori, in *Modern Aspects of Electrochemistry*, (Eds.: C. G. Vayenas, R. E. White, M. E. Gamboa-Aldeco), vol. *42*, Springer, New York, **2008**, pp. 89–189.
[10] Y. Xue, Y. Guo, H. Cui, Z. Zhou, *Small Methods* **2021**, *5*, 2100736.
[11] L. Shang, X. Lv, L. Zhong, S. Li, G. Zheng, *Small Methods* **2021**, *6*, 2101334.
[12] M. Jun, C. Kwak, S. Y. Lee, J. Joo, J. M. Kim, D. J. Im, M. K. Cho, H. Baik, Y. J. Hwang, H. Kim, K. Lee, *Small Methods* **2022**, *6*, 2200074.
[13] D. Higgins, C. Hahn, C. Xiang, T. F. Jaramillo, A. Z. Weber, *ACS Energy Lett.* **2018**, *4*, 317.
[14] H. Rabiee, L. Ge, X. Zhang, S. Hu, M. Li, Z. Yuan, *Energy Environ. Sci.* **2021**, *14*, 1959.
[15] E. F. Johnson, E. Boutin, S. Liu, S. Haussener, *EES Catal.* **2023**, *1*, 704.
[16] N. T. Nesbitt, T. Burdyny, H. Simonson, D. Salvatore, D. Bohra, R. Kas, W. A. Smith, *ACS Catal.* **2020**, *10*, 14093.
[17] B. Endrődi, G. Bencsik, F. Darvas, R. Jones, K. Rajeshwar, Cs. Janáky, *Prog. Energy Combust. Sci.* **2017**, *62*, 133.
[18] L. de Sousa, N. E. Benes, G. Mul, *ACS ES&T Eng.* **2022**, *2*, 2034.
[19] A. Gawel, T. Jaster, D. Siegmund, J. Holzmann, H. Lohmann, E. Klemm, U.-P. Apfel, *iScience* **2022**, *25*, 104011.
[20] M. d. J. Gálvez-Vázquez, P. Moreno-García, H. Xu, Y. Hou, H. Hu, I. Zelocualtecatl Montiel, A. V. Rudnev, S. Alinejad, V. Grozovski, B. J. Wiley, M. Arenz, P. Broekmann, *ACS Catal.* **2020**, *10*, 13096.
[21] L. Hoof, N. Thissen, K. Pellumbi, K. Puring jun., D. Siegmund, A. K. Mechler, U.-P. Apfel, *Cell Rep. Phys. Sci.* **2022**, *3*, 100825.
[22] K. Yang, R. Kas, W. A. Smith, T. Burdyny, *ACS Energy Lett.* **2020**, *6*, 33.
[23] M. Sassenburg, M. Kelly, S. Subramanian, W. A. Smith, T. Burdyny, *ACS Energy Lett.* **2022**, *8*, 321.
[24] S. Garg, Q. Xu, A. B. Moss, M. Mirolo, W. Deng, I. Chorkendorff, J. Drnec, B. Seger, *Energy Environ. Sci.* **2023**, *16*, 1631.
[25] U. O. Nwabara, A. D. Hernandez, D. A. Henckel, X. Chen, E. R. Cofell, M. P. de Heer, S. Verma, A. A. Gewirth, P. J. A. Kenis, *ACS Appl. Energy Mater.* **2021**, *4*, 5175.
[26] M. E. Leonard, L. E. Clarke, A. Forner-Cuenca, S. M. Brown, F. R. Brushett, *ChemSusChem* **2019**, *13*, 400.
[27] M. E. Leonard, M. J. Orella, N. Aiello, Y. Román-Leshkov, A. Forner-Cuenca, F. R. Brushett, *J. Electrochem. Soc.* **2020**, *167*, 124521.
[28] Y. Wu, S. Garg, M. Li, M. N. Idros, Z. Li, R. Lin, J. Chen, G. Wang, Th. E. Rufford, *J. Power Sources* **2022**, *522*, 230998.
[29] L. M. Baumgartner, C. I. Koopman, A. Forner-Cuenca, D. A. Vermaas, *ACS Appl. Energy Mater.* **2022**, *5*, 15125.
[30] B. De Mot, J. Hereijgers, M. Duarte, T. Breugelmans, *Chem. Eng. J.* **2019**, *378*, 122224.
[31] M. Wrobel, S. Kriescher, T. Schiffer, R. Keller, M. Wessling, *Chem. Eng. J.* **2023**, *474*, 145335.
[32] T. Zhang, Z. Li, X. Lyu, J. Raj, G. Zhang, H. Kim, X. Wang, S. Chae, L. Lemen, V. N. Shanov, J. Wu, *J. Electrochem. Soc.* **2022**, *169*, 104506.
[33] Y. Kong, H. Hu, M. Liu, Y. Hou, V. Kolivoška, S. Vesztergom, P. Broekmann, *J. Catal.* **2022**, *408*, 1.
[34] Y. Kong, M. Liu, H. Hu, Y. Hou, S. Vesztergom, M. d. J. Gálvez-Vázquez, I. Zelocualtecatl Montiel, V. Kolivoška, P. Broekmann, *Small Methods* **2022**, *6*, 2200369.
[35] H. Hu, Y. Kong, M. Liu, V. Kolivoška, A. V. Rudnev, Y. Hou, R. Erni, S. Vesztergom, P. Broekmann, *J. Mater. Chem. A* **2023**, *11*, 5083.
[36] M. Liu, H. Hu, Y. Kong, I. Z. Montiel, V. Kolivoška, A. V. Rudnev, Y. Hou, R. Erni, S. Vesztergom, P. Broekmann, *Appl. Catal. B: Environ.* **2023**, *335*, 122885.
[37] S. Vesztergom, A. Senocrate, Y. Kong, V. Kolivoska, F. Bernasconi, R. Zboray, C. Battaglia, P. Broekmann, *Chimia* **2023**, *77*, 104.
[38] A. B. Moss, J. Hätinen, P. Kúš, S. Garg, M. Mirolo, I. Chorkendorff, B. Seger, J. Drnec, *J. Power Sources* **2023**, *562*, 232754.
[39] T. M. M. Heenan, C. Tan, J. Hack, D. J. L. Brett, P. R. Shearing, *Mater. Today* **2019**, *31*, 69.
[40] S. Vesztergom, A. Dutta, M. Rahaman, K. Kiran, I. Zelocualtecatl Montiel, P. Broekmann, *ChemCatChem* **2020**, *13*, 1039.
[41] I. Zelocualtecatl Montiel, A. Dutta, K. Kiran, A. Rieder, A. Iarchuk, S. Vesztergom, M. Mirolo, I. Martens, J. Drnec, P. Broekmann, *ACS Catal.* **2022**, *12*, 10872.
[42] A. Rieder, J. Lorenzetti, I. Zelocualtecatl Montiel, A. Dutta, A. Iarchuk, M. Mirolo, J. Drnec, F. Lorenzutti, S. Haussener, N. Kovács, S. Vesztergom, P. Broekmann, *Zenodo* **2023**, https://doi.org/10.5281/zenodo.10050308.
[43] F. Lorenzutti, S. Haussener, *J. Electrochem. Soc.* **2023**, *170*, 104507.
[44] J. Kieffer, J. P. Wright, *Powder Diffr.* **2013**, *28*, S339.

